Int J Coal Sci Technol (2021) 8(3):335–348
https://doi.org/10.1007/s40789-021-00420-w

Development of new technology for coal gasification purification and research on the formation mechanism of pollutants

Shu Zheng[1] · **Yixiang Shi**[2] · **Zhiqi Wang**[3] · **Pengjie Wang**[4] · **Gang Liu**[4] · **Huaichun Zhou**[5]

Received: 17 June 2020 / Revised: 31 January 2021 / Accepted: 13 March 2021 / Published online: 7 May 2021

Abstract Coal-fired power generation is the main source of CO_2 emission in China. To solve the problems of declined efficiency and increased costs caused by CO_2 capture in coal-fired power systems, an integrated gasification fuel cell (IGFC) power generation technology was developed. The interaction mechanisms among coal gasification and purification, fuel cell and other components were further studied for IGFCs. Towards the direction of coal gasification and purification, we studied gasification reaction characteristics of ultrafine coal particles, ash melting characteristics and their effects on coal gasification reactions, the formation mechanism of pollutants. We further develop an elevated temperature/pressure swing adsorption rig for simultaneous H_2S and CO_2 removals. The results show the validity of the Miura-Maki model to describe the gasification of Shenhua bituminous coal with a good fit between the predicted DTG curves and experimental data. The designed 8–6–1 cycle procedure can effectively remove CO_2 and H_2S simultaneously with removal rate over 99.9%. In addition, transition metal oxides used as mercury removal adsorbents in coal gasified syngas were shown with great potential. The techniques presented in this paper can improve the gasification efficiency and reduce the formation of pollutants in IGFCs.

Keywords IGFC · Coal gasification · H_2S-CO_2 removal · Syngas mercury removal

Abbreviations

AD	Adsorption
AFT	Ash flow temperature
BD	Counter-current blow down
CBK	Carbon burnout kinetic model
CHP	Combined heat and power
DAEM	Distributed activation energy model
DT	Deformation temperature
ETPSA	Elevated temperature pressure swing adsorption
FT	Flow temperature
HT	Hemispherical temperature
IGCC	Integrated gasification combined cycle
IGFC	Integrated coal gasification fuel cell
MDEA	Methyldiethanolamine
PE	Pressure equalization
PG	N_2 purge
PP	Pressurization with product gas
PSA	Pressure swing adsorption
RH	High pressure steam rinse
RPM	Random pore model
SOFC	Solid oxide fuel cell
ST	Softening temperature
TGA	Thermogravimetric analyzer

✉ Shu Zheng
shuzheng@ncepu.edu.cn

[1] National Engineering Laboratory for Biomass Power Generation Equipment, North China Electric Power University, Beijing 102206, China

[2] Key Laboratory for Thermal Science and Power Engineering of Ministry of Education, Department of Energy and Power Engineering, Tsinghua University, Beijing 100084, China

[3] Qingdao Institute of Bioenergy and Bioprocess Technology, Chinese Academy of Sciences, Qingdao 266101, China

[4] State Key Laboratory of Clean Coal-Based Energy, China Huaneng Group Clean Energy Research Institute Co., Ltd., Changping District, Beijing 102209, China

[5] School of Energy and Power Engineering, Northeast Electric Power University, Jilin 132012, China

V	Vacuum desorption
WGS	Water gas shift

Symbols

R	Universal gas constant
A	Pre-exponential factor function
DTG	Predicted combustion reaction rate function
E	Activation energy function
H_g	Hg^0 concentrations [ng/L]
k_0	Pre-exponential factor
K	Reaction rate function
m	Sample weight at time t
m_0	Initial sample weight
m_∞	Final sample weight
R^2	Correlation coefficients
t	Time
T	Temperature

Greek symbols

α	Gasification conversion factor
β	Heating rate
η	Mercury removal efficiency

Subscript

In	Inlet
Out	Outlet

1 Introduction

Integrated coal gasification fuel cell (IGFC) power generation is a combination of integrated gasification combined cycle (IGCC) and solid oxide fuel cell (SOFC) technologies, which could greatly improve the efficiency of coal to electricity and achieve zero emission of CO_2 and pollutants. The SOFC is a critical component in the IGFC. In 2015, Daily (Daily 2015) developed an SOFC power generation system aiming at 5 kW and reached a power output of 4.82 kW. Its power generation and CHP efficiency were 48.5% and 79.7%, respectively. SOFCMAN developed an SOFC of 200 kW in 2016 (Sofcman 2016). Another SOFC power generation system of 15 kW was established by Shanxi Jincheng Anthracite Coal Mining Group in China (Li and Zhang 2019). In 2017, China approved an IGFC project and planned to build a MWth level demonstration station within four years, with a power efficiency higher than 50% and CO_2 capture rate higher than 91% (Dong et al. 2019). The SOFC technology has been industrialized overseas as well. For example, Bloom Energy, Mitsubishi and Convion are able to produce SOFCs of 30–200 kW (Cao et al. 2020). Base on the development of SOFC technology, many counties have made plans to promote the development and application of IGFC. In 2015, Japan (Strategy 2019) planned to establish an IGFC power generation of 100 MW with power efficiency of 55% before 2025. In United States, the company Fuel Cell Energy planned to establish a demonstration IGFC station of 670 MW (Cao et al. 2020). IGFC is regarded as the most promising near-zero CO_2 emission coal gasification power generation technology in the future (Peng and Han 2009).

The entrained-bed coal gasification process is the cleanest and most efficient coal gasification technology (Fan 2013; Liu et al. 2010; Wang 2014). At present, the entrained-bed coal gasification process is widely used in IGCC power stations over 250 MW (Zhang and Yang 2019). Compared with fixed-bed and fluidized-bed gasifiers, entrained-bed gasifiers have the advantages of coal adoptability and operation reliability. The entrained-bed gasifiers used in China nowadays mainly include Texaco, Shell and GSP gasifiers. How to improve the carbon conversion rate and cold gas efficiency has been a key difficulty in the entrained-bed coal gasification technology.

Entrained flow coal gasification technology, whose carbon conversion rate and cold gas efficiency can be as high as 98% and 80% respectively, represents a direction of coal gasification. Liquid slagging and dry feeding coal gasification technology has many advantages such as low oxygen consumption, high carbon conversion, high cold gas efficiency and large capacity for single furnace, which will be a mainstream of advanced coal gasification (Liu and Tian 2012). Pulverized coal with low ash melting point is often used in dry feeding entrained flow gasification. Gasifying temperatures should be higher than ash melting point to ensure the liquid ash removal (Krishnamoorthy and Pisupati 2015). The successful development of large energy efficient ultrafine pulverized coal preparation system establishes the foundation for the utilization of ultrafine pulverized coal. Microscale effect of ultrafine pulverized coal can increase the gasification rate and conversion efficiency (Liu et al. 2014; Luo et al. 2019). This paper intends to review the research on gasification characteristics of ultrafine pulverized coal under CO_2 atmosphere and to describe the basic kinetic characteristics of ultrafine pulverized coal, so as to provide theoretical guidance for improved effective gas yield, carbon conversion rate and cold gas efficiency.

At present, the general coal gasification reaction model does not consider the thermal deactivation effect of coal at high temperatures, high pressures and high conversion rates. The most commonly used kinetic models for coal gasification reaction include homogeneous model, core-shrinking reaction model and random hole model. Homogeneous model can only describe a process in which the rate of gasification reaction decreases monotonously with the rate of carbon conversion. However, it is not applicable to the gasification process with extreme gasification reaction rates. Although the stochastic pore model can describe the extreme gasification reaction rates, it is not suitable to describe the catalytic gasification process of coal and the extreme value of gasification reaction rate occurs in the case of high conversion rate. So far, no model can accurately describe the process of gasification reaction rate changing with reaction time and conversion rate. Therefore, the establishment of a generalized and quantitative kinetic model to describe coal gasification reaction will be the focus of coal gasification reaction dynamics research.

The distributed activation energy model (DAEM) (Pitt 1962) and carbon burnout kinetic model (CBK) (Cloke et al. 2003; Hurt et al. 1998)have been proven very successful for describing the kinetics of coal pyrolysis and combustion. The DAEM was originally proposed by Pitt (Pitt 1962) and later adapted by Anthony and Howard (Anthony and Howard 1976). It describes a complex reaction as a number of parallel first-order reactions, each occurring with its own rate coefficient. Usually, it is further assumed that all reactions share the same frequency factor and that measuring the relationship between the distributed activation energy and the burnout ratio requires at least three different heating rates. The CBK model was proposed by Hurt (1998). It accurately describes the kinetics of heterogeneous char oxidation reactions. One of the main limitations of this type of research is that burning and burnout temperatures are always lower than the ash flow temperature (AFT). The kinetic characteristics of coal high-temperature combustion require further investigation. In this study, the kinetic parameters of char combustion including the activation energy (E) and the pre-exponential factor (A) were obtained from thermogravimetric analyzer (TGA) data. A model that predicted the char combustion rate was then established using the kinetic parameters of char combustion and was validated with experimental data.

Combustion of syngas (mixtures of H_2 and CO) can greatly reduce CO_2 emissions in power generation systems (Sui et al. 2018, 2019, 2020a). In the field of syngas purification, there are several industrialized methods that could separately remove H_2S and CO_2, such as Selexol, methyldiethanolamine (MDEA), rectisol and pressure swing adsorption (PSA) (Chaubey et al. 2013; Dincer and Acar 2015; Wiheeb et al. 2013; Yu et al. 2012). These techniques are widely used in coal chemical industry, providing a basis for the development of H_2S-CO_2 simultaneous removal methods. Selexol, rectisol and MDEA belong to the category of wet methods, in which impurities are absorbed by solvents at - 50 – 60 °C. The solvent in MDEA is a chemical absorbent while the others are physical absorbents. The devices of wet methods are complicated and costly. Impurity removal and absorbents regeneration are conducted in different units. The maintenance and operating costs are not economical either.

Consequently, some substitutes of conventional purification methods are proposed and studied. Using dry methods, RTI international (Denton 2014; Gupta and Raghubir 2010) separated H_2S and CO_2 from syngas at elevated temperatures and normal temperatures, respectively, with more than 99.9% H_2S and 90% CO_2 captured. Compared with Selexol and rectisol, the initial investment of this method decreased by 50% and the operating cost was also lower. The energy consumption of adsorbent/absorbent regeneration was only 72% of that in Selexol. Moreover, if H_2S and CO_2 could be simultaneously removed in one step, the device can be further simplified. Still, the corresponding techniques are under development. Improvement of adsorbent performance, technique process design and adsorption bed structure optimization are all necessary at this stage.

With the rapid development of human society, energy and environmental problems are becoming more and more serious. The fact that China is rich in coal resources but poor in oil and natural gas determines that coal will be the main fossil energy source to maintain the rapid development of the whole society in a long period of time. Accordingly, sulfur, nitrogen, chlorine and other pollutants generated in the processes of coal utilization have been widely concerned (Xu and Wei 1999); The trace and volatile metal elements (such as Hg, Pb, As, Se, etc.) has also been paid more attention. Mercury is the most volatile heavy metal pollutant in coal. Although its concentration in coal is relatively low, considering the total consumption of coal is huge and mercury is mainly discharged in the form of gas, the latter in the process of coal utilization accounts for a large proportion of the mercury released by human activities.

With increased attention paid to mercury pollution in the atmosphere, mercury emission in the processes of coal utilization has become an urgent environmental problem. There are three forms of mercury released from coal utilization: Hg^p, Hg^{2+} and Hg^0. Hg^p can be removed by particulate control and Hg^{2+} can be removed by wet scrubbing or SO_2 control, while elemental mercury is not easy to dissolve, making it difficult to be removed via ordinary dust removal equipment (Pavlish et al. 2003). In the recent years, the research works of mercury removal are mainly focused on the removal of mercury from coal-fired flue gas. The main methods are: (1) adsorption method: adsorption of mercury in flue gas with activated carbon, fly ash, mineral adsorbents, etc. (Granite et al. 2000; Liu 2015); (2) catalytic adsorption method: metal oxides (such as TiO_2, CeO_2, ZnO, MoO_3, Cuo, MnO_2, etc.) (Li et al. 2011; Liu 2016; Wen et al. 2011) or precious metals (Ag, Pd, Pt, etc.) (Liu et al. 2008) are loaded on Al_2O_3 or molecular sieve and other carriers to remove mercury. The two methods show a certain ability of mercury removal in different temperature ranges, while the components of flue gas (SO_2, SO_3, NO, NO_x, HCl, etc.) have a great influence on the mechanism of mercury removal. The gases produced by coal gasification are composed of reducing agents (usually containing trace O_2) and the content of elemental mercury that is difficult to remove is higher than that of coal-fired flue gases (Pavlish et al. 2003; Reed et al. 2001). Therefore, the removal of mercury from coal gas exhausts has gradually become a research hotspot at home and abroad.

The paper is organized as follows: in Sect. 2, coal gasification models and syngas purification methods are presented. Subsequently, in Sect. 3, experiments and calculations of CO_2 gasification of ultrafine pulverized coal particles, H_2S-CO_2 removal and syngas mercury removal are discussed. Finally, the conclusions are summarized in Sect. 4.

2 Methods and experiments

2.1 Kinetic models of coal gasification

Bituminous coal obtained from Shenhua mine was used in this work. Screening equipment was used to separate materials with five particle sizes, whose average particle sizes were determined by Malvern Mastersizer 3000. Thermogravimetric analysis was conducted via a TG (Setsys Evolution, SETARAM, France). Each sample was heated in CO_2 environment from ambient temperature to 1300 °C with four different heating rates (5, 10, 20, and 40 °C/min). The integral iso-conversional model proposed by Miura-Maki (Miura and Maki 1998) has been widely used to obtain kinetic parameters for thermal-conversion of coal. The previous work (Song et al. 2016) proved the validity of Miura-Maki model by comparing the experimental and the reproduced conversion degree versus temperature based on the calculated kinetic parameters.

$$\ln\left(\frac{\beta}{T^2}\right) = \ln\left(\frac{K_0 R}{E}\right) + 0.6075 - \frac{E}{RT} \tag{1}$$

where, β is the heating rate, k_0 is the pre-exponential factor, E is the activation energy, R is the universal gas constant.

At low operating temperatures, the chemical reaction rates are slow and the oxygen supply rate is much faster than the oxygen consumption rate. Therefore, the combustion process consisted of a slow heating zone and a combustion reaction zone, which can be considered a dynamic area where chemical kinetic factors control the reaction rate (Sun and Chen 1991). The reaction rate can be expressed with the Arrhenius with the following assumptions (Zhang et al. 2000):

(1) The sample particles are spherical. The particle diameter and density are constant during the combustion process. The impact of the ash layer on the combustion is not considered.
(2) The combustion reactions only occur on the particles' surfaces and the reaction rate is calculated based on the particles' outside surface area.
(3) The oxygen pressure is distributed evenly throughout the sample layer.
(4) The total surface oxidation reaction product is CO_2.

The combustion rate function can be expressed as follows (Hecker et al. 2003; Sima-Ella et al. 2005):

$$\alpha = \frac{m_0 - m}{m_0 - m_\infty} \tag{2}$$

$$-\frac{d\alpha}{dt} = K(\alpha)\alpha \tag{3}$$

The reaction rate function $K(\alpha)$ is usually assumed via the Arrhenius equation (Pilling and Seakins 1995):

$$K(\alpha) = A(\alpha)\exp(-E(\alpha)/(RT)) \tag{4}$$

where, α is the burnout ratio, which is the mass ratio of the burned combustible matter to the total combustible matter in the coal. m_0 is the initial mass weight of the sample and m is the sample's mass weight at time t. m_∞ is the final sample weight. $K(\alpha)$ is the combustion reaction rate as a function of α. $A(\alpha)$ is the pre-exponential factor function and $E(\alpha)$ is the activation energy function.

The curves of char combustion at two temperatures T_1 and T_2 can be obtained from TGA experiments including $TG_1(\alpha)$, $TG_2(\alpha)$, $DTG_1(\alpha)$, and $DTG_2(\alpha)$. $E(\alpha)$ and $A(\alpha)$ from T_1 to T_2 can be calculated as:

$$E_{T_1-T_2}(\alpha) = -\frac{R\ln\frac{DTG_1(\alpha)}{DTG_2(\alpha)}}{\left(\frac{1}{T_1} - \frac{1}{T_2}\right)} \tag{5}$$

$$A_{T_1-T_2}(\alpha) = \frac{DTG_2(\alpha)}{\exp(-E_{T_1-T_2}(\alpha)/(RT_2))} \tag{6}$$

From Eqs. (5) and (6), the predicted combustion reaction rate function $DTG'(\alpha)$ at a combustion temperature of T_3 ($T_3 \in [T_1, T_2]$) is as follows:

$$DTG'(\alpha) = A_{T_1-T_2}(\alpha)\exp(-E_{T_1-T_2}(\alpha)/RT_3) \tag{7}$$

To validate the predicted model's veracity, the predicted results are compared with experimental data and an error analysis is conducted.

Hulunbeier lignite coal was utilized in the present work. The average diameter of the coal samples was 76 µm and all samples were less than 200 µm. The coal properties, ash components, and fusion characteristic temperatures are presented in Table 1.

Table 1 Coal properties (as received basis, wt%) and ash components analysis

Item	Value	Item	Value
Coal proximate analysis (wt%)		Ash compositions (wt%)	
Fixed carbon	44.86	SiO_2	55.63
Volatile matter	35.44	Al_2O_3	11.51
Ash	11.05	Fe_2O_3	14.22
Moisture	8.65	CaO	11.24
Ultimate analysis		MgO	2.14
(wt%)		TiO_2	0.76
Carbon	59.46	SO_3	3.02
Hydrogen	3.35	P_2O_5	0.06
Oxygen	16.44	K_2O	0.48
Nitrogen	0.80	Na_2O	0.94
Sulfur	0.25	Fusion characteristic temperature	
Lower heating value	25.6	(°C)	1090
(MJ/kg)		DT[a]	
		ST[b]	1100
		HT[c]	1110
		FT[d]	1160

[a] Deformation Temperature.

[b] Softening Temperature.

[c] Hemispherical Temperature.

There were four adsorption[d] Flow Temperature

A TGA from Beijing Henven Scientific Instrument Factory was used. The minimum sensitivity was 0.1 μg and the data was collected every second in a temperature range of 25 °C to 1450 °C.

All coal samples were measured with 20 mg, dewatered at 100 °C for 30 min and heated at a fixed heating rate of 80 °C/min, starting from 100 °C and rising to the temperature T_H in N_2 environment (200 mL/min). The samples were then held at T_H for 30 min for complete volatile devolatilization. Air (100 mL/min) was injected into the TGA after 30 min and the temperature was kept constant until the mass weights of the samples remained constant. The temperature T_H in each case was divided into 25 levels in the range of 500–1450 °C, with heating intervals of 50 °C in the range of 500–1200 °C and 25 °C in the range of 1200–1450 °C.

2.2 H_2S-CO_2 removal

The authors had proposed elevated temperature pressure swing adsorption (ETPSA) process operating at 150–400 °C for H_2S-CO_2 simultaneous removal. It is similar to PSA but with higher working temperatures. As a dry method, the device of ETPSA is less complex than that in wet methods. Furthermore, compared with regular PSA, ETPSA is more energy efficient due to a higher product gas recovery rate and less sensible heat loss (Gazzani et al. 2013).

A small scale (6 Nm^3/h) ETPSA unit has been developed in in the ammonia plant of Quanji Energy Co., Ltd., Shanxi province, China. On-site CO_2-H_2S simultaneous removal is realized on this device. Syngas coming for water gas shift [WGS, which converts CO to CO_2 for pre-combustion capture (Sui et al. 2020b)] unit flowed to this unit with a flow rate of 1 – 10 Nm^3/h. The WGS is approximately 50 m away from ETPSA, and hence the temperature decreased from 216 °C to around 180 °C during the transport. A part of the steam was condensed and separated by a gas–liquid separator. The compositions of final feed gas are listed in Table 2.

There were four adsorption beds and four buffer tanks (same size columns packed with SiO_2 particles of similar sizes) in this rig. The tanks were used for pressure equalization. The height of adsorption beds were 1.8 m and the inner diameter was 79 mm. The adsorbent was 207C activated carbon (Calgon Carbon Co., Ltd.), which had undergone some special surface treatment (Li et al. 2019). The hydrophobicity of the adsorbent was significantly higher than the pristine activated carbon. The outlook of this rig is shown in Fig. 1.

According to elevating the working temperature, the reversibility of H_2S adsorption was improved (Hao et al. 2019). Adsorbed H_2S could be detached from the adsorbent and collected during vacuum desorption or purge step. Although the sulfur capacity of activated carbon was lower than metal oxides, the breakthrough times of H_2S was still much longer than CO_2. Hence as long as CO_2 did not penetrate the adsorption bed, the H_2S could be removed thoroughly.

Herein, an 8–6–1 (eight adsorption beds/tanks, six pressure equalization, one adsorption in each cycle) ETPSA cycles were designed. The schedules are shown in Fig. 2, where the step sequence and the corresponding duration lengths are listed. The time length of each cycle here is 468 s (the last line in the chart). Because N_2 is a material of ammonia synthesis, N_2 purging was adopted in this study.

Table 2 Details of the feed gas

Temperature	Pressure	Composition
180 °C	2–3 MPa	54% H_2, 36% CO_2, 5% H_2O, 0.4% CO, 700 ppm H_2S, 1% N_2, 3% CH_4, Trace Ar

2.3 Syngas mercury removal

The precursor $Mn(NO_3)_2 \cdot 4H_2O$ of 10 g manganese oxide was dissolved in deionized water in a 100 ml bottle, creating a 100 mL $Mn(NO_3)_2$ solution with a mass fraction of 10 wt.% 0.10 g activated alumina and 10 mL manganese nitrate aqueous. Then the activated alumina was added to manganese nitrate aqueous solution, stirred manually for 30 min, and followed by ultrasonic shock for 20 min. The activated alumina impregnated with manganese nitrate solution was heated in the electric furnace of 200 W and was placed in the oven at 100 °C for 1 h until water was fully evaporated. After drying, alumina loaded with manganese oxide precursor was placed in a tubular furnace at a constant temperature of 400 °C and removed after calcining for 3 h in air. Subsequently, it was cooled to room temperature in a drying dish. The obtained Mn_2O_3/Al_2O_3 mercury removal adsorbent was stored in silica gel. Similarly, Co_2O_3/Al_2O_3 and Fe_2O_3/Al_2O_3 adsorbents were prepared by the same method with $Co(NO_3)_2$ and $Fe(NO_3)_2$ as precursors, respectively.

The experiment was carried out in the fixed bed reactor system, as shown in Fig. 3. The apparatus mainly includes 6 parts: simulated syngas control system, mercury vapor generation system, water vapor generation system, tubular reactor system, tail gas treatment system and mercury analysis system. An MAX-L cold atomic absorption mercury analyzer produced by Labtech Company was used in the experiments to access the mercury concentrations.

The mercury removal activity of the adsorbent was evaluated in a fixed bed reactor at 200 °C in a simulated gas (N_2, CO, H_2, H_2S, H_2O and Hg) environment. The experimental apparatus is shown in Fig. 4. The simulated gas was selected in the experiment. Hg steam concentration was 60 $\mu g/m^3$. The stable concentration was provided by mercury permeation tube through the dynamic gas calibration instrument. The permeation temperature was set at 60 °C. The carrier gas was N_2 and the flow rate was 200 mL/min. The simulated gas was provided by standard gas distribution cylinders with H_2S concentration of 200 ppm, H_2 volume fraction of 30%, CO volume fraction of 60%, CO_2 volume fraction of 5% and H_2O vapor volume fraction of 5%. The total gas flow rate was 1 L/min (nitrogen as the equilibrium gas). The adsorbent dose was 0.5 g and the bed temperature was set as 200 °C.


Small-scale pilot of PSA at elevated temperature at Fengxi Ammonia Plant

Fig. 1 Outlook photo of the ETPSA device

The mercury removal efficiency (ŋ) of the adsorbent was used as the evaluation index, whose calculation formula was as follows:

$$\eta = \frac{H_{\mathrm{gin}} - H_{\mathrm{gout}}}{H_{\mathrm{gin}}} \tag{8}$$

where, H_{gin} and H_{gout} denote the inlet and outlet Hg^0 concentrations (ng/L), respectively.

3 Results and discussions

3.1 CO_2 gasification of ultrafine pulverized coal particles

It can be seen from the particle size distribution curves (as shown in Fig. 5a) and microscopic appearance (as shown in Fig. 5b) that the average particle sizes for Samples 1#, 2# and 3# were smaller than Samples 4# and 5#. Further, the surfaces of 4# and 5# was smooth, while the surfaces of 1#, 2# and 3# was rather rough. The rough surfaces would promote the gasification process and enhance the reaction activity. The gasification conversion factor (α) curves for the five samples with different particle sizes (as shown in Fig. 5c) almost overlapped when the temperature was lower than 850 °C. However, when the temperature was higher than 850 °C, there existed significant differences for coal samples with different particle sizes. As for the effect of particle size on the gasification conversion factor, it can be found that the smaller the particle size, the larger value of conversion factor. According to the plot of $\ln(\beta/T^2)$ vs $1/T$ at a particular conversion factor (α) (as shown in Fig. 5d), a linear equation with the slope of $-E/R$ and intercept of $\ln(k_0R/E) + 0.6075$ can be fitted, which gives the values of activation energies, pre-exponential factors, and correlation coefficients (R^2). The calculated values of correlation coefficient for all the five samples were all higher than 0.97, showing that the Miura-Maki model is applicable to Shenhua bituminous coal for gasification kinetic analysis.

3.2 Predicted DTG model

Figure 6 depicts the $T(t)$, $1-\alpha(t)$, DTG(t), and DTG(α) profiles for the Hulunbeier lignite coal. As shown in Fig. 6

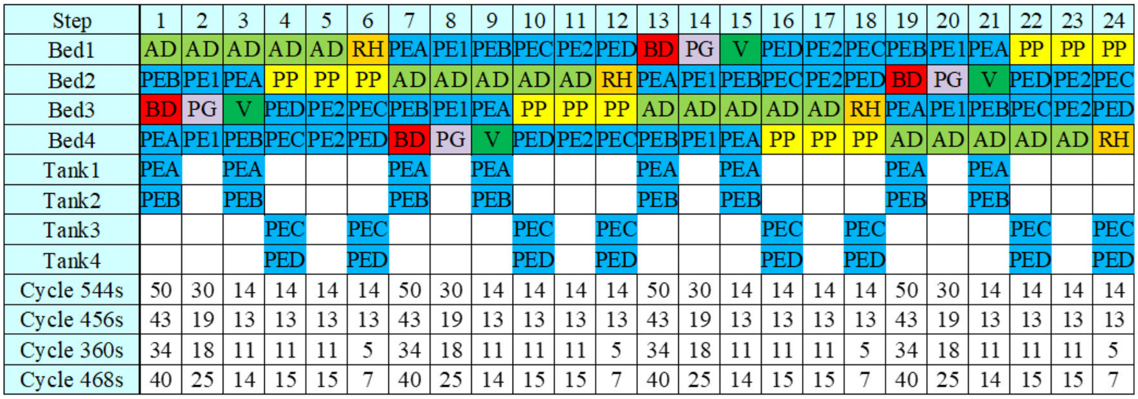

Step	1	2	3	4	5	6	7	8	9	10	11	12	13	14	15	16	17	18	19	20	21	22	23	24
Bed1	AD	AD	AD	AD	AD	RH	PEA	PE1	PEB	PEC	PE2	PED	BD	PG	V	PED	PE2	PEC	PEB	PE1	PEA	PP	PP	PP
Bed2	PEB	PE1	PEA	PP	PP	PP	AD	AD	AD	AD	AD	RH	PEA	PE1	PEB	PEC	PE2	PED	BD	PG	V	PED	PE2	PEC
Bed3	BD	PG	V	PED	PE2	PEC	PEB	PE1	PEA	PP	PP	PP	AD	AD	AD	AD	AD	RH	PEA	PE1	PEB	PEC	PE2	PED
Bed4	PEA	PE1	PEB	PEC	PE2	PED	BD	PG	V	PED	PE2	PEC	PEB	PE1	PEA	PP	PP	PP	AD	AD	AD	AD	AD	RH
Tank1	PEA		PEA				PEA		PEA				PEA		PEA				PEA		PEA			
Tank2	PEB		PEB				PEB		PEB				PEB		PEB				PEB		PEB			
Tank3				PEC		PEC				PEC		PEC				PEC		PEC				PEC		PEC
Tank4				PED		PED				PED		PED				PED		PED				PED		PED
Cycle 544s	50	30	14	14	14	14	50	30	14	14	14	14	50	30	14	14	14	14	50	30	14	14	14	14
Cycle 456s	43	19	13	13	13	13	43	19	13	13	13	13	43	19	13	13	13	13	43	19	13	13	13	13
Cycle 360s	34	18	11	11	11	5	34	18	11	11	11	5	34	18	11	11	11	5	34	18	11	11	11	5
Cycle 468s	40	25	14	15	15	7	40	25	14	15	15	7	40	25	14	15	15	7	40	25	14	15	15	7

Fig. 2 8–6–1 ETPSA cycle procedures. AD: adsorption; RH: high pressure steam rinse; PE: pressure equalization with columns (1, 2) or tanks (A, B, C, D); BD: counter-current blow down; PG: N_2 purge; V: vacuum desorption; PP: pressurization with product gas

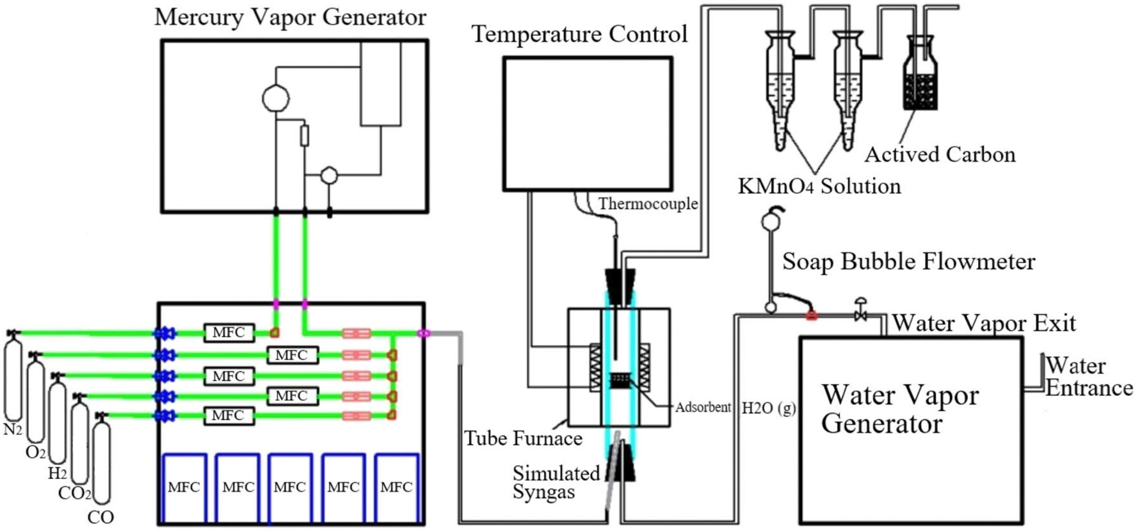

Fig. 3 Schematic diagram of simulated syngas mercury removal system

b and c, the weight loss ratio *1–α* and the reaction rate DTG(*t*) exhibit a regular distribution as the combustion temperature increases. The peaks in the DTG(α) profiles shown in Fig. 6 d can be observed when the burnout ratio α is around 0.1, which was also observed by Bhatia et al. (Bhatia and Perlmutter 1980). The authors proposed a random pore model (RPM), which stated that the reaction rate responded to the change in pore structure and that a positive relationship existed between changes in the reaction rate and pore superficial area. The changes in the pore superficial area were the result of the competition between the pore extension and the pore overlap. The pore extension benefited from the increase in pore superficial area while the result for the pore overlap was the opposite. At the beginning of char combustion, the pore extension dominated and the reaction rate increased rapidly with the rising pore superficial area. After the peak of the reaction rate, which occurred at α_{max}, the pore overlap began to dominate the reaction and the reaction rate decreased with the reduction in the pore superficial area. The peak of the reaction rate predicted by the RPM occurred at $0 < \alpha_{max} < 0.393$, which matched the observations shown in Fig. 6d.

E(α) and *A*(α) are obtained by Eqs. (5) and (6) and are shown in Fig. 7. The result shows that both *E*(α) and log *A*(α) exhibited a U-shaped with a gentle fluctuation in the range of $0.2 < \alpha < 0.9$. As the burnout ratio increased from 0 to 0.3, the char began to burn and the combustion rate increased significantly. This resulted in the decrease in *E* and log *A*. As the combustion continued, the flammable matter burned first and heated the flame retardant matter. The combustion rate, *E*, and log *A* were relatively stable in the range of $0.2 < \alpha < 0.9$. As the combustion temperature increased from 500 °C to 1200 °C, *E* and log *A* curves progressively decreased in the range of $0.2 < \alpha < 0.9$ and increased in the range of 1200–1450 °C. At the end of the

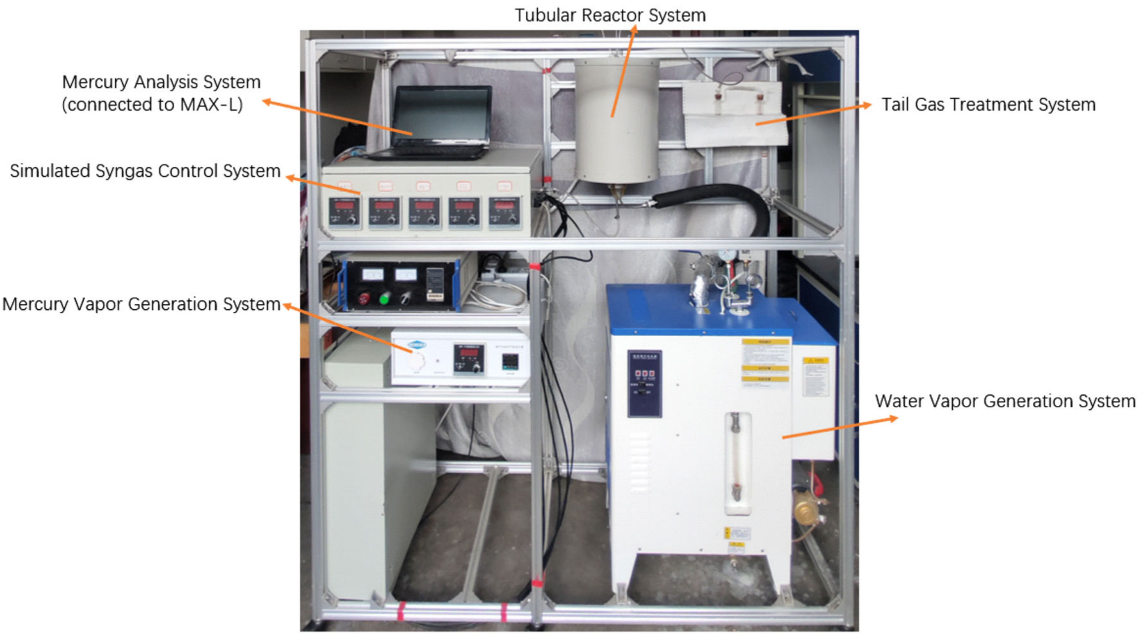

Fig. 4 Test bench of syngas mercury removal system

combustion $0.9 < \alpha < 1$, E and log A curves increased exponentially for all temperatures.

The E and log A curves were stable in the range of $0.2 < \alpha < 0.9$ and mean E and log A in this range are shown in Fig. 8. At a combustion temperature lower than the AFT (1160 °C), the E and log A values fluctuated within the same order of magnitude. However, when the combustion temperature exceeded the AFT, the E and log A values increased exponentially. It is noteworthy that the mean E and A values in the range of $0.2 < \alpha < 0.9$ varied with different temperatures, especially when the combustion temperature exceeded the AFT.

The values of T_1 and T_2 were identified as close as possible to avoid the effect of the AFT on the results of E and A. Using Eqs. (5), (6), and (7), DTG'α at a combustion temperature of T_3 ($T_3 = (T_1 + T_2)/2$) was obtained. The comparisons of the predicted and experimental results are shown in Fig. 9a. Figure 9b shows the error analysis for the range of $0.2 < \alpha < 0.9$. The predicted DTG curves fit the experimental data well. The maximum and mean relative errors were less than 6.5% and 2.5%, respectively. This indicated that the DTG predicted model proposed in this study was validated to predict the char combustion in the TGA; the model performed especially well for high-temperature ($T > 1200$ °C) char combustion.

3.3 H_2S-CO_2 removal

The compositions of the product gas are listed in Table 3. Steam was removed via cooling before the evaluation. It is seen that the concentration of CO_2 was lower than 500 ppm, attesting 99.9% of CO_2 was captured by the adsorbent. The concentration of H_2S was lower than the detection accuracy of chromatographic (0.1 ppm). Hence, H_2S removal by activated carbon seems to be feasible. After running for several months, H_2S did not penetrate the adsorption bed, indicating the adsorption of H_2S did be reversible. As a physical adsorbent, activated carbon could more or less adsorb all kinds of gas. Therefore, not only CO_2 and H_2S but also CO and CH_4 were partially removed during this process. Because N_2 was adopted as the purging gas, the concentration of N_2 is higher than the feed gas. Small amount of inert gas is acceptable when H_2 is used in IGCC and IGFC.

The H_2 recovery rate during this purification process is 97%, which is much higher than regular PSA (Lopes et al. 2011; Shen et al. 2012; Wang et al. 2012). It could be attributed to the introduction of vacuum desorption and steam rinse. In order to explore the influence of rinse and vacuum desorption, we changed the cycle procedure and evaluated the corresponding product gas compositions and recovery rates. The case shown above is the best one and is named as Case 4 and the others are marked Case 1–3. The results are as shown in Table 4 for comparisons. The conditions and parameters were same as Case 4 if not specifically mentioned. We regulated the cycle time to make the product purity close Case 4 so that the recovery rate could represent the separation efficiency. The time length of each step is also given in Fig. 2.

After replacing V and RH with PG and AD, respectively, the H_2 recovery decreased to 79.3%, which was close to some regular PSA operated at normal temperatures

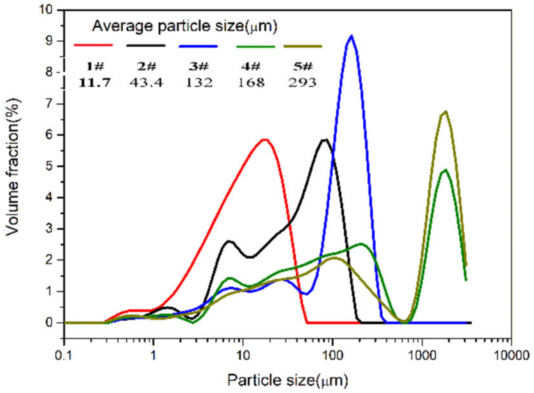

(**a**) particle size distribution curves

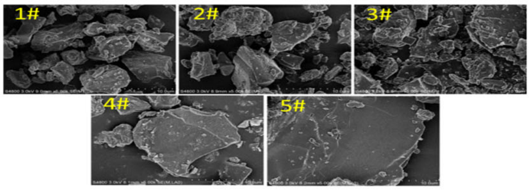

(**b**) the micro surface morphology

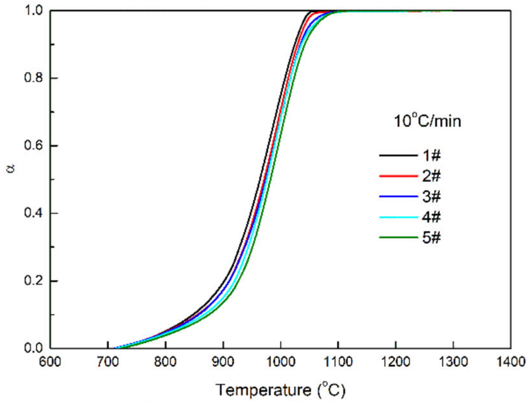

(**c**) gasification conversion factor curves

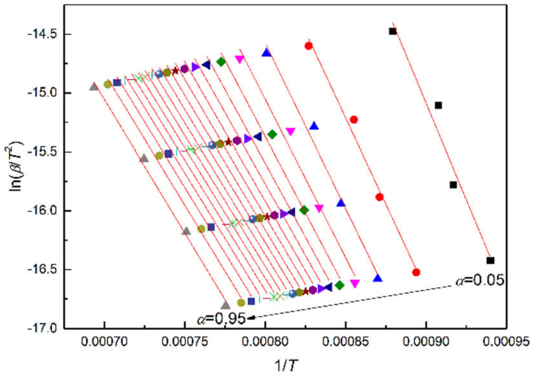

(**d**) the plots of $\ln(\beta/T^2)$ vs 1/T

Fig. 5 Experimental results of five coal samples with different particle sizes: **a** particle size distribution curves, **b** micro surface morphology, **c** gasification conversion factor curves and **d** the plots of $\ln(\beta/T^2)$ vs $1/T$ at a particular conversion factor

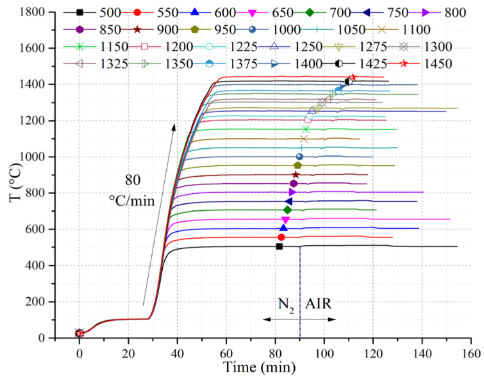

(**a**) $T(t)$

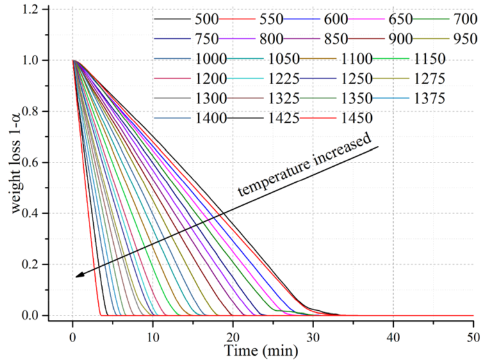

(**b**) $1\text{-}\alpha(t)$

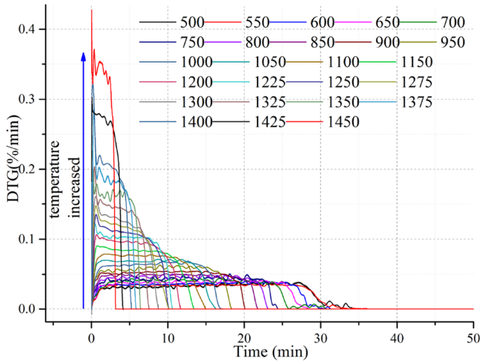

(**c**) DTG(t)

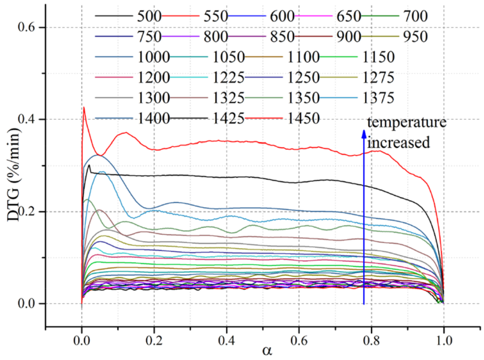

(**d**) DTG(α)

Fig. 6 **a** $T(t)$, **b** $1\text{–}\alpha(t)$, **c** DTG(t), and **d** DTG(α) profiles for the Hulunbeier lignite coal

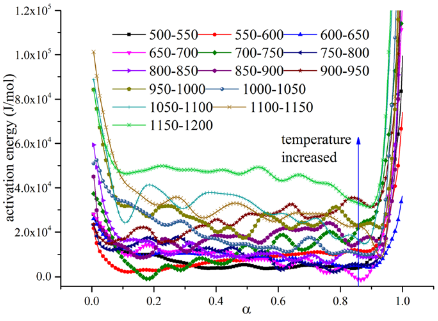

(a) activation energy $E(\alpha)$ within the temperature of 500-1200 °C

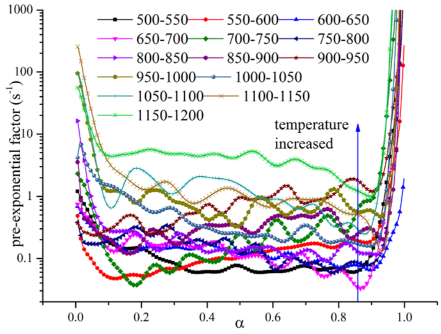

(b) pre-exponential factor $A(\alpha)$ within the temperature of 500-1200 °C

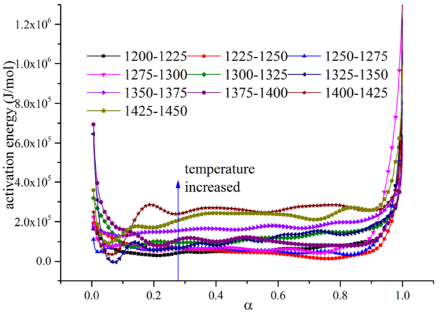

(c) activation energy $E(\alpha)$ within the temperature of 1200-1450 °C

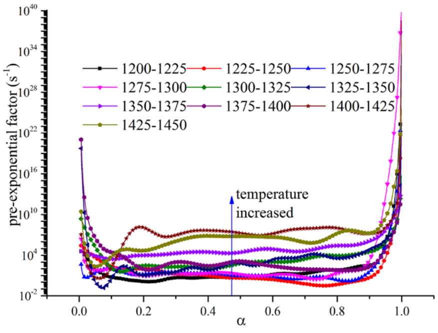

(d) pre-exponential factor $A(\alpha)$ within the temperature of 1200-1450 °C

Fig. 7 The results for **a** activation energy $E(\alpha)$ and **b** pre-exponential factor $A(\alpha)$

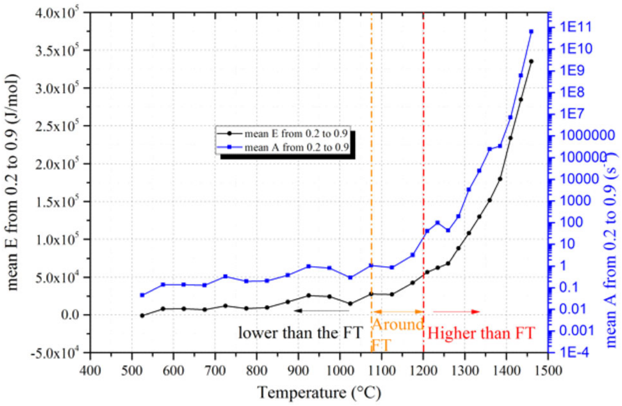

Fig. 8 Mean E and A values in the range of $0.2 < \alpha < 0.9$

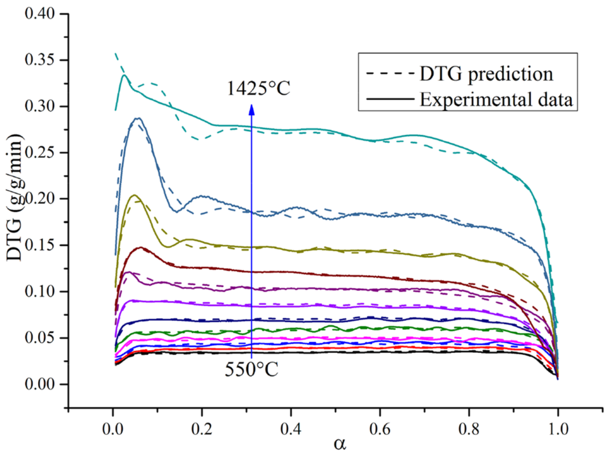

(a) DTG predicted and experimental results

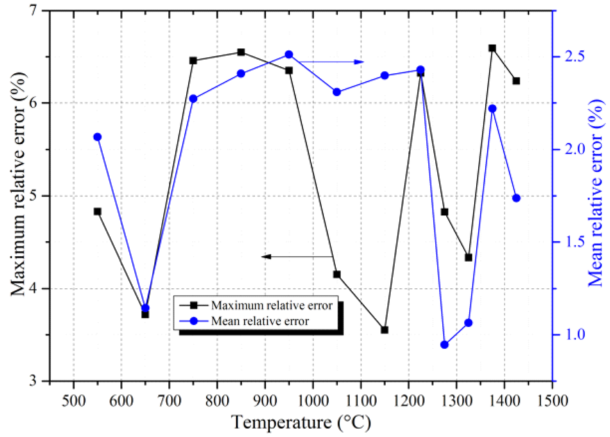

(b) Error analysis in the range of $0.2 < \alpha < 0.9$.

Fig. 9 Comparisons of **a** DTG predicted and experimental results and **b** error analysis in the range of $0.2 < \alpha < 0.9$

(Mivechian and Pakizeh 2013; Rahimpour et al. 2013). Considering the adsorption capacity of activated carbon could deteriorate with the rising temperature, we set the temperature as 120 °C and the H_2 recovery rate is thus

Table 3 Working condition and purification outcomes of 8–6–1 ETPSA

Temperature	Pressure	Flow rate	Product gas composition (dry)
170 °C	2 MPa	5.7 Nm^3/h	1%–2% N_2, < 500 ppm CO_2, < 0.1% CO, < 0.1 ppm H_2S, < 100 ppm CH_4, H_2 as balance gas

improved in Case 2. Subsequently, steam rinse was added and H_2 recovery increased to over 90% immediately. This means steam rinse was a significant factor. However, although the cycle time of Case 3 is shorter, CO_2 concentration in product gas was up to 0.3%, which was much higher than Case 4. It was mainly due to the remained impurities in adsorption bed after regeneration steps. Vacuum desorption is demonstrated to be effective in promoting adsorbent regeneration and hence compensates the defect in desorption kinetic performance. The introduction of vacuum desorption results in extra power consumption and the cost of high pressure steam in rinse step will also lead to more energy consumption. Consequently, the energy efficiency of ETPSA should be further discussed in our following studies.

3.4 Syngas mercury removal

3.4.1 *α-Al_2O_3 measurement*

α-Al_2O_3 was selected as the carrier in the experiments, with the parameters as shown in Table 5. It can be seen that specific surface area of α-Al_2O_3 may reach as high as 237 m^2/g. Such a large value manifested α-Al_2O_3 as an ideal carrier material.

3.4.2 *Mercury removal test of the carrier*

Mercury removal experiments were carried out at different temperatures with α-Al_2O_3, which was not impregnated with the active component. The experimental result are shown in Fig. 10. It could be seen that at the temperature of 150 °C mercury removal efficiency was about 5%. Counter-intuitively, mercury removal efficiency decreased with the increase of temperature. When the temperature reached 400 °C, the mercury removal efficiency was almost zero. The reason was probably because α-Al_2O_3 was full of the microchannel and had very large specific surface area, which possessed strong physical adsorption capacity. Therefore, α-Al_2O_3 presented the mercury removal capacity in lower temperature, but does not possess chemical adsorption capacity and the mercury removal capacity was lost when the temperature reached 400 °C.

Table 5 Properties of the carrier α-Al_2O_3

Sample	Size (mm)	specific surface area (m^2/g)
α-Al_2O_3	1.5	237

3.4.3 *Evaluation of prepared adsorbents*

The prepared Mn_2O_3/Al_2O_3, Co_2O_3/Al_2O_3 and Fe_2O_3/Al_2O_3 loaded with active components were evaluated individually under the simulated gas condition at 200 °C. The evaluation results are shown in Figs. 11 and 12.

As shown in Figs. 11 and 12, the mercury removal efficiency of the prepared Mn_2O_3/Al_2O_3 could reach 90.4% in the first 10 min, and then slowly decreased and finally dropped to a stable.

level at ~ 60%. The initial mercury removal efficiency of the prepared Co_2O_3/Al_2O_3 was 86%, and the final mercury removal efficiency was stable at about 60%. The mercury removal agent Fe_2O_3/Al_2O_3 had the best mercury removal performance, with its initial mercury removal efficiency reaching 95.4%. In the two-hour test, the mercury removal agent was maintained at about 90% with no attenuation.

It could be seen in Figs. 11 and 13 that the mercury removal efficiency of Mn_2O_3/Al_2O_3 and Co_2O_3/Al_2O_3 both showed very big promotion compared to pure Al_2O_3, indicating the original physical adsorption was changed and could suggesting that physical adsorption and chemical adsorption synergy effected co-existed (Huo et al. 2017; Mao et al. 2018). The mechanism was speculated as follows (Mn_2O_3 as example):

$$Mn_2O_3 + 3H_2 \rightarrow 2Mn^2 + 3H_2O \qquad (9)$$

Table 4 Separation efficiencies of different cases with and without vacuum desorption and steam rinse

Case	Temperature (°C)	Flow rate (Nm^3/h)	Cycle time (s)	H_2S (ppm)	CO_2	H_2 recovery	Procedure
1	170	5.2	456	< 0.1	~ 0.3%	79.3%	Without V and RH
2	120	6.8	544	< 0.1	~ 0.3%	86.4%	Without V and RH
3	170	5.7	360	< 0.1	~ 0.3%	93.3%	Without V

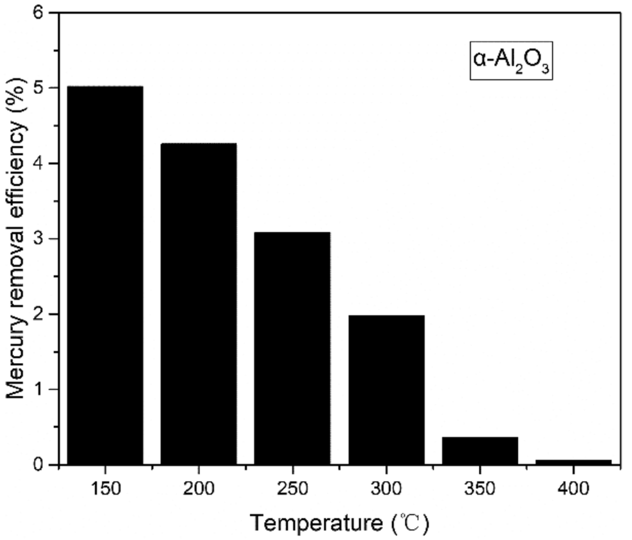

Fig. 10 Mercury removal performance of α-Al_2O_3 at different temperatures

$$Mn_2O_3 + 3CO \rightarrow 2Mn^0 + 3H_2O \quad (10)$$

$$Mn^2 + H_g^0 \rightarrow Mn - H_g \quad (11)$$

Meanwhile, the mercury removal efficiency of Mn_2O_3/Al_2O_3 and Co_2O_3/Al_2O_3 both displayed the trend of decreasing during 2 h test. Finally, the mercury removal efficiency was stabilized at a certain value, suggesting that the reaction of Hg^0 and the active component reached reaction equilibrium.

The mercury removal mechanism of Fe_2O_3/Al_2O_3 was obviously different from that of Mn_2O_3/Al_2O_3 and Co_2O_3/Al_2O_3. The mechanism was proposed as follows:

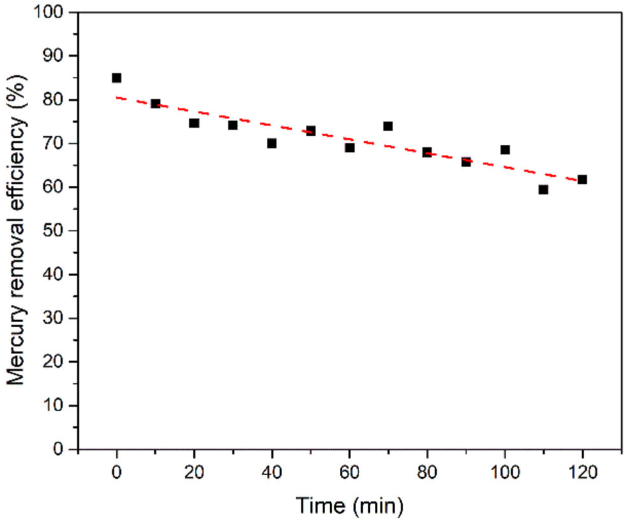

Fig. 12 The test curve of mercury removal performance of Fe_2O_3/Al_2O_3

$$3H_2S + Fe_2O_3 \rightarrow 2FeSx + Sad + 3H_2O \quad (12)$$

$$H_g^0 + Sad \rightarrow H_gS \quad (13)$$

It could be seen that because of its existence in coal gasification syngas, H_2S improved the mercury removal efficiency and stability of Fe_2O_3/Al_2O_3 mercury removal agent. Hence, H_2S replaced the combination of transition metal oxides with Hg^0, making its mercury removal efficiency reached more than 90%.

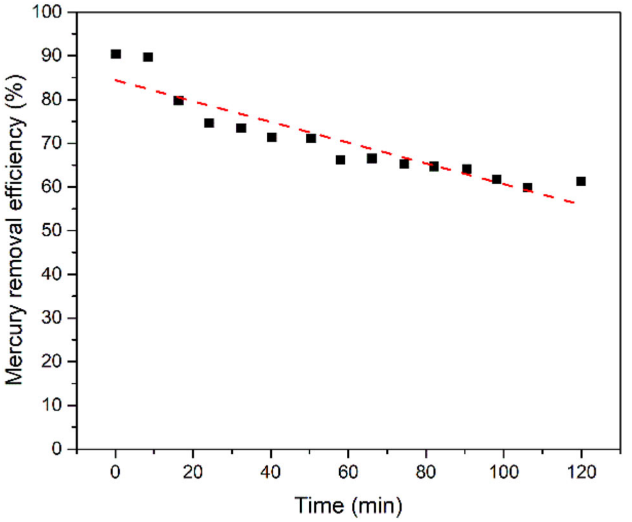

Fig. 11 Test curve of mercury removal performance of Mn_2O_3/Al_2O_3

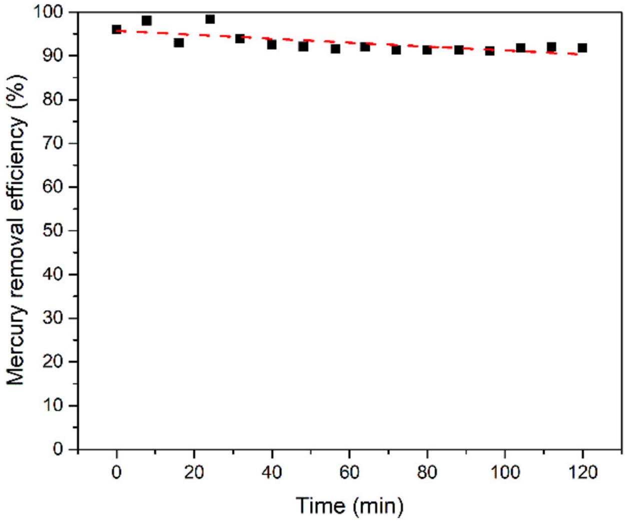

Fig. 13 Test curve of mercury removal performance of Co_2O_3/Al_2O_3

4 Conclusions

In this paper, the gasification reaction characteristics of ultrafine coal particles, the formation mechanism of pollutants, and H_2S and CO_2 simultaneous removal in the process of IGFC were studied. The following conclusions can be obtained.

(1) The surface became coarser with the decrease of coal sample particle size, which could promote the gasification process and improve the reaction activity. The gasification kinetic parameters of Shenhua bituminous coal were obtained from the Miura-Maki Model. The value of activation energy decreased with reducing particle size of the coal samples.

(2) A database of the kinetic characteristics functions of char combustion and a DTG model was established. The maximum and mean relative errors were less than 6.5% and 2.5%, respectively. The predicted DTG curves fit the experimental data well because the effect of the AFT on the E and A values was taken into account.

(3) A small scale ETPSA rig was built in an ammonia plant and on-site syngas H_2S-CO_2 simultaneous removal was realized. An 8–6–1 cycle procedure with steam rinse and vacuum desorption was designed and demonstrated to be efficient. The concentration of CO_2 and H_2S in the product gas was lower than 500 ppm and 0.1 ppm, respectively, indicating a removal rate over 99.9%. The corresponding H_2 recovery rate was 97%. The importance of steam rinse and vacuum desorption was verified after changing the cycle procedure. However, the energy efficiency of ETPSA should be analyzed in detail in future studies.

(4) Three kinds of mercury removal adsorbents were prepared, Mn_2O_3/Al_2O_3, Co_2O_3/Al_2O_3 and Fe_2O_3/Al_2O_3, which showed diverse degrees of mercury removal performance. Among them, the mercury removal efficiency of Fe_2O_3/Al_2O_3 was basically stable at more than 90% under the 2 h condition at 200 °C medium temperature test. The use of transition metal oxides as mercury removal adsorbents in coal gasification syngas had great potential and was hence the main direction of the research on mercury removal in IGFC gas purification system.

Acknowledgements This work was financially supported by National Key R&D Program of China (2017YFB0601900).

References

Anthony DB, Howard JB (1976) Coal devolatilization and hydrogastification. AIChE J 22(4):625–656

Bhatia SK, Perlmutter D (1980) A random pore model for fluid-solid reactions: I Isothermal, kinetic control. AIChE J 26(3):379–386

Cao J, Wang X, Sun X, Luo Z (2020) High-efficiency clean power generation system based on solid oxide fuel cell. Southern Energy Construct 7(02):28–34

Chaubey R, Sahu S, James OO, Maity S (2013) A review on development of industrial processes and emerging techniques for production of hydrogen from renewable and sustainable sources. Renew Sustain Energy Rev 23:443–462

Cloke M, Wu T, Barranco R, Lester E (2003) Char characterisation and its application in a coal burnout model. Fuel 82(15):1989–2000

Daily CS (2015) Huazhong University of Science and Technology has developed a solid oxide fuel cell independent power generation system

Denton, L D (2014) An update on RTI's warm syngas cleanup demonstration project. Paper presented at the Gasification Technologies Conference, Washington, DC

Dincer I, Acar C (2015) Review and evaluation of hydrogen production methods for better sustainability. Int J Hydrogen Energy 40(34):11094–11111

Dong B, Li C, Huang B, Liu C, Wang Q, Fan W, Li P (2019) Integrated gasification fuel cell power generation technology with CO_2 near zero emission and its challenges. Coal Sci Technol 47(07):189–193

Fan W (2013) Comparison of coal water slurry and coal dust feeding methods of entrained flow gasification technology. Clean Coal Technol 19(003):71–73

Gazzani M, Macchi E, Manzolini G (2013) CO2 capture in integrated gasification combined cycle with SEWGS—Part A: Thermodynamic performances. Fuel 105:206–219

Granite EJ, Pennline HW, Hargis RA (2000) Novel sorbents for mercury removal from flue gas. Ind Eng Chem Res 39(4):1020

Gupta, Raghubir (2010) Scaleup and Commercialization of Warm Syngas Cleanup Technology with Carbon Capture and Storage. Paper presented at the Gasification Technologies Conference, Washington, DC

Hao P, Liu Z, Shi Y, Li S, Cai N (2019) Characteristics of activated carbon in elevated-temperature pressure swing adsorption desulfurization. Adsorption 25(6):1–8

Hecker WC, Madsen PM, Sherman MR, Allen JW, Sawaya RJ, Fletcher TH (2003) High-pressure intrinsic oxidation kinetics of two coal chars. Energy Fuels 17(2):427–432

Huo Q, Qi D, Ye L, Han L, Chang L (2017) The preparation of PdFe/Al_2O_3 mercury removal sorbent by chemical co-precipitation. Chem React Eng Technol 33(5):450–457

Hurt R, Sun J-K, Lunden M (1998a) A kinetic model of carbon burnout in pulverized coal combustion. Combust Flame 113(1):181–197

Krishnamoorthy V, Pisupati SV (2015) A critical review of mineral matter related issues during gasification of coal in fixed, fluidized, and entrained flow gasifiers. Energies 8(9):10430–10463

Li H, Wu CY, Li Y, Zhang J (2011) CeO_2-TiO_2 catalysts for catalytic oxidation of elemental mercury in low-rank coal combustion flue gas. Environ Sci Technol 45(17):7394–7400

Li S, Hao P, Zhu X, Shi Y, Jiang H (2019) On-site demonstration of an elevated temperature hydrogen clean-up unit for fuel cell applications. Adsorption 25(8):1683–1693

Li Y, Zhang H (2019) Construction and operation of carbon based fuel cell SOFC power generation demonstration project of Shanxi Jincheng Anthracite Coal Mining Group. Energy Technol Manage 044(005):153–156

Liu B, Tian J (2012) Progress in effects of coal properties on entrained-flow gasification. Chem Ind Eng Prog 31(10):2191–2196

Liu J, Jiang X, Han X, Shen J, Zhang H (2014) Chemical properties of superfine pulverized coals. Part 2. Demineralization effects on free radical characteristics. Fuel 115:685–696

Liu T (2016) Mechanism and experimental study on removal of elemental mercury by iron oxide. Dissertation, Huazhong University of Science and Technology

Liu X (2015) Theoretical study of removal of .γ-Al_2O_3 for hydrogen sulfide and mercury. Dissertation, Taiyuan University of Technology

Liu X, Tian Y, Qiao Y (2010) Progress of entrained-bed coal gasificaton technology. Chem Ind Eng Prog 29(S2):120–124

Liu Y, Kelly DJA, Yand H, Lin CCH, Kuznicki SM, Xu Z (2008) Novel Regenerable sorbent for mercury capture from flue gases of coal-fired power plant. Environ Sci Technol 42(16):6205–6210

Lopes FVS, Grande CA, Rodrigues AE (2011) Activated carbon for hydrogen purification by pressure swing adsorption: Multicomponent breakthrough curves and PSA performance. Chem Eng Sci 66(3):303–317

Luo L, Yao W, Liu J, Zhang H, Ma J, Jiang X (2019) The effect of the grinding process on pore structures, functional groups and release characteristic of flash pyrolysis of superfine pulverized coal. Fuel 235:1337–1346

Mao J, Zhou J, Li X, Zhou Q, Cao H (2018) Mechanism of mercury removal in syngas by co-modified activated coke with H_2S. Chin J Appl Chem 35(12):106–115

Miura K, Maki T (1998) A simple method for estimating f(E) and k0(E) in the distributed activation energy model. Energy Fuels 12(5):864–869

Mivechian A, Pakizeh M (2013) Hydrogen recovery from Tehran refinery off-gas using pressure swing adsorption, gas absorption and membrane separation technologies: simulation and economic evaluation. Korean J Chem Eng 30(4):937–948

Pavlish JH, Sondreal EA, Mann MD, Olson ES, Benson SA (2003) Status review of mercury control options for coal-fired power plants. Fuel Process Technol 82(2):89–165

Pilling MJ, Seakins PW (1995) Reaction Kinetics. Oxford University Press, New York

Pitt G (1962) The kinetics of the evolution of volatile products from coal. Fuel 41(3):267–274

Rahimpour MR, Ghaemi M, Jokar SM, Dehghani O, Jafari M, S.Amiri, S.Raeissi (2013) The enhancement of hydrogen recovery in PSA unit of domestic petrochemical plant. Chem Eng J Lausanne

Reed GP, Ergudenler A, Grace JR, Watkinson AP, Herod AA, Dugwell D, Kandiyoti R (2001) Control of gasifier mercury emissions in a hot gas filter: the effect of temperature. Fuel 80(5):623–634

Shen C, Liu Z, Li P, Yu J (2012) Two-stage VPSA process for CO_2 capture from flue gas using activated carbon beads. Ind Eng Chem Res 51:5011–5021

Sima-Ella E, Yuan G, Mays T (2005) A simple kinetic analysis to determine the intrinsic reactivity of coal chars. Fuel 84(14):1920–1925

Sofcman (2016) SOFCMAN sets a world record in stack module performance

Song H, Liu G, Wu J (2016) Pyrolysis characteristics and kinetics of low rank coals by distributed activation energy model. Energy Convers Manage 126:1037–1046

Strategy CAoESd (2019) Report on the Development of China's Strategic Emerging Industries in 2020

Sui R, Es-sebbar E, Mantzaras J, Prasianakis NI (2018) Experimental and numerical investigation of fuel-lean H_2/CO/air and H_2/CH_4/air catalytic microreactors. Combust Sci Technol 190(2):336–362

Sui R, Liang W, Mantzaras J, Law CK (2020a) Coupled reaction mechanism reduction for the hetero-/homogeneous combustion of syngas over platinum. Combust Flame 214:37–46

Sui R, Liang W, Zhang L, Mantzaras J, Law CK (2020b) Kinetic interactions between H_2 and CO in catalytic oxidation over PdO. Combust Flame 211:270–280

Sui R, Mantzaras J, Es-sebbar E, Bombach R (2019) Hetero-/homogeneous combustion of fuel-lean CH_4/O_2/N_2 mixtures over PdO at elevated pressures. Proc Combust Inst 37(4):5465–5472

Sun X, Chen J (1991) Physical and chemical basis of pulverized coal combustion. HUST Press, Wuhan

Wang B (2014) Chemistry and technology progress of coal gasification. Clean Coal Technol 20(003):69–74

Wang L, Liu Z, Li P, Wang J, Yu J (2012) CO_2 capture from flue gas by two successive VPSA units using 13XAPG. Adsorption 18(5–6):445–459

Wen X, Li C, Fan X, Gao H, Zhao Y (2011) Experimental study of gaseous elemental mercury removal with CeO_2/y-Al_2O_3. Energy Fuels 25(7):2939–2944

Wiheeb AD, Shamsudin IK, Ahmad MA, Murat MN, Kim J, Othman MR (2013) Present technologies for hydrogen sulfide removal from gaseous mixtures. Rev Chem Eng 29(6):449–470

Xu S, Wei S (1999) An analysis and evaluation of the gas clean-up process equipment and technical equipment characteristics in four IGCC demonstration power plants. Clean Coal Technol 5(1):47–51

Yu CH, Huang CH, Tan CS (2012) A review of CO_2 capture by absorption and adsorption. Aerosol Air Quality Res 12(5):745–769

Zhang X, Nie Q, Sun S (2000) A study of thermobalance model for the burning of blended coals. J Eng Thermal Energy Power 15(4):356–359

Zhang Y, Yang Q (2019) Development status and trend of coal gasification technology. Chem Enterprise Manage 25(S2):7–13